



Observation of Fano line shape in directional fluorescence emission mediated by coupled planar waveguide modes and interpretation based on Lorentz reciprocity

Kang, Byungjun ; Motokura, Kengo ; Fujii, Minoru ; Nesterenko, Dmitry, V ; Sekkat, Zouheir ; Hayashi, Shinji

(Citation)

AIP Advances, 10(7):075302-075302

(Issue Date)

2020-07-01

(Resource Type)

journal article

(Version)

Version of Record

(Rights)

© 2020 Author(s).

All article content, except where otherwise noted, is licensed under a Creative Commons Attribution (CC BY) license (<http://creativecommons.org/licenses/by/4.0/>).

(URL)


<https://hdl.handle.net/20.500.14094/90007452>



Observation of Fano line shape in directional fluorescence emission mediated by coupled planar waveguide modes and interpretation based on Lorentz reciprocity

Cite as: AIP Advances 10, 075302 (2020); <https://doi.org/10.1063/5.0010930>

Submitted: 16 April 2020 . Accepted: 12 June 2020 . Published Online: 01 July 2020

Byungjun Kang, Kengo Motokura, Minoru Fujii , Dmitry V. Nesterenko , Zouheir Sekkat , and Shinji Hayashi 

COLLECTIONS

Paper published as part of the special topic on [Chemical Physics](#), [Energy](#), [Fluids and Plasmas](#), [Materials Science](#) and [Mathematical Physics](#)



View Online



Export Citation



CrossMark

ARTICLES YOU MAY BE INTERESTED IN

[Wide-range line shape control of Fano-like resonances in all-dielectric multilayer structures based on enhanced light absorption in photochromic waveguide layers](#)

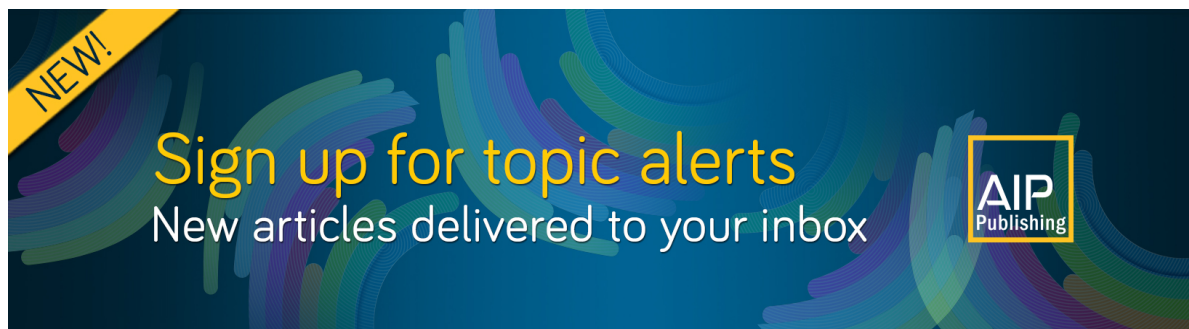
Journal of Applied Physics **127**, 073103 (2020); <https://doi.org/10.1063/1.5131681>

[Simulation of photochemically induced motion of matter in gradient light fields](#)

Journal of Applied Physics **127**, 243106 (2020); <https://doi.org/10.1063/5.0011388>

[Light-controllable Fano resonance in azo-dye-doped all-dielectric multilayer structure](#)

Journal of Applied Physics **125**, 223101 (2019); <https://doi.org/10.1063/1.5091820>



Observation of Fano line shape in directional fluorescence emission mediated by coupled planar waveguide modes and interpretation based on Lorentz reciprocity

Cite as: AIP Advances 10, 075302 (2020); doi: 10.1063/5.0010930

Submitted: 16 April 2020 • Accepted: 12 June 2020 •

Published Online: 1 July 2020



Byungjun Kang,¹ Kengo Motokura,¹ Minoru Fujii,¹ Dmitry V. Nesterenko,^{2,3} Zouheir Sekkat,^{4,5,6} and Shinji Hayashi^{1,4,a)}

AFFILIATIONS

¹Department of Electrical and Electronic Engineering, Graduate School of Engineering, Kobe University, Kobe 657-8501, Japan

²Image Processing Systems Institute RAS—Branch of the FSRC “Crystallography and Photonics” RAS, Samara 443001, Russia

³Faculty of Information Technology, Samara National Research University, Samara 443086, Russia

⁴Optics and Photonics Center, Moroccan Foundation for Science, Innovation and Research (MAScIR), Rabat 10100, Morocco

⁵Faculty of Sciences, Mohamed V University in Rabat, Rabat 10010, Morocco

⁶Graduate School of Engineering, Osaka University, Suita 565-0871, Japan

^{a)} Author to whom correspondence should be addressed: s.hayashi@dragon.kobe-u.ac.jp

ABSTRACT

Using a reverse attenuated-total-reflection geometry, we measured angle-scan fluorescence emission spectra of all-dielectric multilayer samples containing a waveguide layer doped with fluorescent dye molecules (fluorescent waveguide layer). A sample containing only one fluorescent waveguide layer showed a highly directional emission spectrum with a Lorentzian line shape caused by the radiative decay of an excited planar waveguide mode into a traveling wave in a decoupling prism. Addition of another waveguide layer containing absorptive dye molecules was found to greatly modify the spectrum and generate a Fano line shape in the emission spectrum. The observed Lorentzian and Fano emission spectra could be well reproduced by electromagnetic calculations based on the Lorentz reciprocity theorem. Calculated results of electric field distributions indicate that the Fano line shape is generated by the suppression of local electric fields inside the fluorescent waveguide layer resulting from coupling between two waveguide modes.

© 2020 Author(s). All article content, except where otherwise noted, is licensed under a Creative Commons Attribution (CC BY) license (<http://creativecommons.org/licenses/by/4.0/>). <https://doi.org/10.1063/5.0010930>

It has long been known that spontaneous emission of an emitter can be modified by the structure of the emitter's environment since the spontaneous emission is not an intrinsic property of the emitter.¹ At the early stage of research, a lot of experimental and theoretical studies have been performed on the emission of fluorophores placed in the vicinity of metal–dielectric interfaces, where the excitation of surface plasmon polaritons (SPPs) plays an important role.^{2,3} Highly directional enhanced emission realized by surface plasmon-coupled emission in a reverse attenuated total reflection (ATR) geometry attracted considerable interest because of its potential applications

in fluorescence-based biosensing.^{4–6} Over the past two decades, great efforts have been made to control the decay rate, spectral shape, and directionality of emission from nanoemitters such as fluorescent dye molecules and quantum dots by placing them close to or inside photonic nanostructures, including plasmonic and dielectric nanostructures, photonic crystals, and metamaterials.^{7–11} Of particular interest has been the integration of nanoemitters into photonic nanostructures that exhibit Fano resonances in far-field optical responses. For a variety of Fano-resonant nanostructures combined with nanoemitters, asymmetric Fano-type emission spectra were observed^{12–18} and

intensity enhancements were also demonstrated.^{13,15–20} Since tailoring the Fano-resonant nanostructure allows the generation of high-Q resonances associated with large field enhancements and also allows us to engineer the line shape and directionality of light emission, the Fano-type emission of emitters integrated in the Fano-resonant nanostructures is very much promising for developing effective light sources, biosensors, platforms of enhanced spectroscopies, and so on. However, there exist only a few reports. Behaviors of local electric fields at the positions of emitters, which play crucial roles in generating the Fano line shape, are not yet well analyzed, and the mechanisms of Fano line shape generation in emission spectra are not yet well known. Further experimental and theoretical studies on Fano-type emission are highly required to push forward the Fano-resonant nanostructures toward real applications.

In the present work, we choose an all-dielectric multilayer structure to realize the Fano-type fluorescence emission spectra. In our previous studies, we demonstrated the feasibility of generating high-Q Fano resonances in angle-scan ATR spectra for metal-dielectric^{21–26} and all-dielectric^{27–29} multilayer structures. The ATR Fano line shapes observed are manifestations of Fano-resonant behaviors of absorption resulting from coupling between a broad SPP mode and a sharp planar waveguide (PWG) mode and between a sharp PWG mode and a broad PWG mode. Very recently, we also

observed Fano line shapes in the fluorescence excitation spectra of an all-dielectric multilayer structure incorporating a waveguide layer doped with fluorescent dye molecules; the observed line shapes also reflect the Fano-resonant behaviors of absorption inside the dye-doped waveguide layer at the wavelength of excitation light.³⁰ In this letter, taking maximum advantage of simplicity in the sample preparation, high controllability of optical responses, and feasibility in analytical electromagnetic (EM) calculations, and extending our previous work on the fluorescence *excitation* spectra, we give clear experimental evidence of Fano line shapes in fluorescence *emission* spectra. We used a reverse ATR geometry very similar to that used for observing surface plasmon-coupled emission.^{4–6} In the present geometry, the emission line shape reflects the Fano-resonant behavior of local electric fields inside the fluorescent waveguide layer. We demonstrate that the observed line shape can be well reproduced by EM calculations based on the Lorentz reciprocity theorem.

The multilayer sample shown in Fig. 1(a) was prepared on a SF11 glass substrate by a spin-coating method. The sample is almost the same as that used in our previous study.³⁰ A polystyrene (PS) layer doped with 4-(dicyanomethylene)-2-methyl-6-(4-dimethylaminostyryl)-4H-pyran (DCM) molecules (DCM-PS layer) plays the role of the light emitting waveguide layer (WG1 layer). To deposit the layer, a toluene solution of 7 wt. % PS

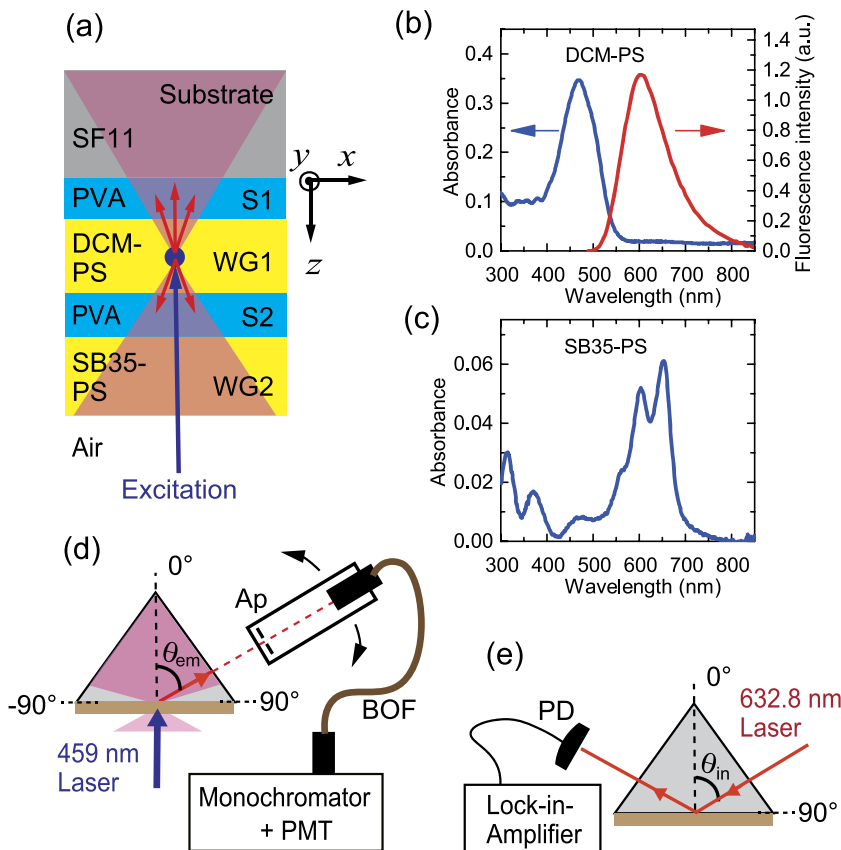


FIG. 1. (a) Prepared multilayer sample. (b) Absorption and fluorescence spectra of a single polystyrene layer doped with DCM molecules. (c) Absorption spectrum of a single polystyrene layer doped with SB35 molecules. (d) Reverse ATR geometry for fluorescence emission measurements. Ap and BOF stand for aperture and bundle optical fiber, respectively. (e) ATR geometry for reflection measurements.

containing DCM molecules (3 wt. % relative to PS) was spun with a rotation speed of 3800 rpm on a polyvinyl alcohol (PVA) spacer layer (S1 layer) deposited by spinning a 4 wt. % water solution with a speed of 5000 rpm. After depositing the second PVA spacer layer (S2 layer) by spinning a 6 wt. % solution with a speed of 2500 rpm, the sample was completed by depositing the second waveguide layer (WG2 layer). As for the WG2 layer, we used a PS layer containing absorptive dye molecules, solvent blue 35 (SB35-PS layer); a toluene solution of 7 wt. % PS containing SB35 molecules (0.2 wt. % relative to PS) was spun with a speed of 1800 rpm. Figure 1(b) shows a typical absorption spectrum and a fluorescence spectrum of a single DCM-PS layer deposited on a glass substrate, measured by using a UV-visible spectrometer (SHIMADZU UV-3101PC) and a spectrofluorometer (HORIBA Fluorolog-3), respectively. We see that the DCM-PS layer exhibits a broad absorption band peaking around $\lambda = 470$ nm with a full width at half maximum of ~ 100 nm and a broad fluorescence band peaking around $\lambda = 600$ nm with a full width at half maximum of ~ 115 nm. In Fig. 1(c), a typical absorption spectrum of a single SB35-PS layer deposited on a glass substrate is shown. We see that the SB35-PS layer shows a broad absorption band in the green-red spectral region. In the sample prepared, the WG1 and WG2 layers can support planar waveguide modes, PWG1 and PWG2 modes, respectively. We call the sample the coupled-waveguide (CWG) sample. As a control sample, we also prepared a multilayer stack not containing the WG2 layer. The control sample is called the single-waveguide (SWG) sample.

Fluorescence emission spectra were measured in a reverse ATR configuration schematically shown in Fig. 1(d), which is very similar to that used in surface plasmon-coupled emission observations.^{4–6} The multilayer sample was pasted onto a 60°-SF11 prism with the aid of index matching fluid. An excitation beam from a laser diode with a wavelength of $\lambda_{\text{ex}} = 459$ nm, which is very close to the wavelength of the absorption maximum of the DCM-PS layer [Fig. 1(b)], was incident normal to the sample surface from the air side and focused into a spot ~ 500 μm in diameter. The polarization of the excitation beam was set to the y direction in the coordinate system shown in Fig. 1(a). The fluorescence emitted into the prism side was collected by a bundle optical fiber 1.5 mm in diameter mounted on a computer-controlled rotational arm and sent to a monochromator. Setting the monochromator to pass light at $\lambda_{\text{em}} = 633$ nm with a width of ~ 10 nm, the intensity of emitted light was measured by a photon counting method using a photomultiplier, as a function of the rotational angle of the arm. The external angle of the arm was converted to the internal angle θ_{em} (emission angle) inside the SF11 prism defined in Fig. 1(d), and the angle-scan emission spectra were obtained as a function of θ_{em} . It should be noted that the directions of excitation and observation of the fluorescence emission in the present work are totally reversed relative to those in our previous work;³⁰ the present study is aimed to study the fluorescence *emission* process totally different from the absorption process that governed the previous fluorescence *excitation* spectra. In this paper, we present only s -polarized (s -pol.) emission spectra since p -polarized spectra showed that essentially, the line shapes and conclusions drawn are the same as those for s -pol. spectra. The ATR spectra of the samples were measured in a manner described in our previous papers^{26,27} using a 632.8 nm probe beam from a He-Ne laser, as

schematically shown in Fig. 1(e). The thicknesses and refractive indices of the layers were determined by fitting experimental ATR spectra to the theoretical ones.

The fluorescence emission of the SWG sample is characterized by highly directional emission into the prism, as shown in Fig. 2(a); we see sharp distributions of emission around $\theta_{\text{em}} = \pm 60^\circ$ for $\lambda_{\text{em}} = 633$ nm. Although no metallic layer exists in our sample, the observed directional emission is very similar to those reported for surface plasmon-coupled emission.^{4–6} Figure 2(b), in which the emission intensity is plotted for positive values of θ_{em} , demonstrates that the emission band exhibits a Lorentzian shape with a full width at half maximum (FWHM) of $\sim 0.86^\circ$. In exactly the same manner as surface plasmon-coupled emission, the directional emission observed for the SWG sample is explained by the excitation of the PWG1 mode by fluorophore radiation and successive radiative decay of the excited PWG1 mode into the prism. In the reverse ATR configuration, for a fixed emission wavelength λ_{em} , the emission is allowed only around θ_{em} that satisfies the phase matching condition $k_x(\lambda_{\text{em}}) = n_p(2\pi/\lambda_{\text{em}}) \sin \theta_{\text{em}}$, where $k_x(\lambda_{\text{em}})$ is the in-plane wavevector of the PWG1 mode and n_p is the refractive index of the prism ($n_p = 1.7786$ at $\lambda_{\text{em}} = 633$ nm for SF11). The width of the emission band is determined by the intrinsic and radiative losses of the PWG1 mode. The solid line shown in Fig. 2(b) is a theoretical curve explained later in this paper.

The addition of the WG2 layer to form the CWG sample strongly modifies the emission spectrum, as demonstrated in Fig. 2(c). A pronounced asymmetric dip appears in the emission band. In the supplementary material, a p -pol. emission spectrum observed is shown in Fig. S1. The spectrum in Fig. S1 demonstrates that the characteristic features of the line shape observed for the

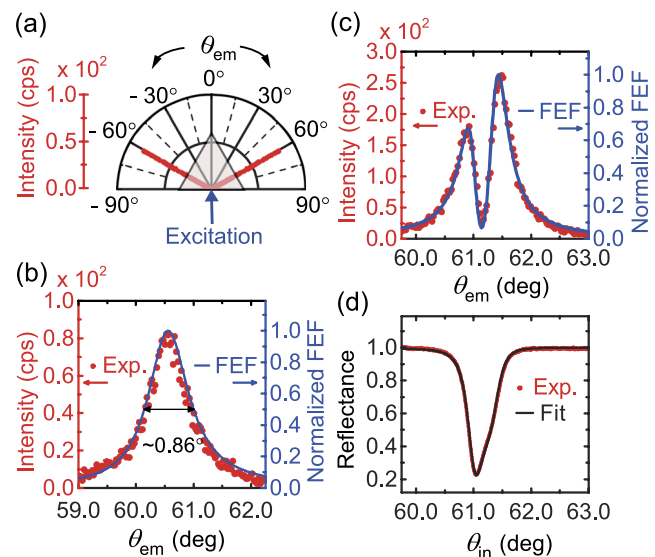


FIG. 2. (a) Polar plot of fluorescence intensities for the SWG sample. (b) Experimental and calculated angle-scan fluorescence emission spectra for the SWG sample. (c) Experimental and calculated angle-scan fluorescence emission spectra for the CWG sample. (d) Experimental ATR spectrum and theoretical fit curve for the CWG sample.

TABLE I. Structural parameters determined from the theoretical fit of ATR spectra.

Layers	SWG sample		CWG sample	
	Thickness (nm)	Refractive index	Thickness (nm)	Refractive index
S1	105	$1.5030 + i1.0 \times 10^{-5}$	109	$1.4930 + i1.0 \times 10^{-5}$
WG1	520	$1.5866 + i6.0 \times 10^{-5}$	627	$1.5913 + i2.0 \times 10^{-5}$
S2	1000	$1.5270 + i1.0 \times 10^{-5}$	524	$1.5242 + i1.0 \times 10^{-5}$
WG2	740	$1.5851 + i7.9 \times 10^{-4}$

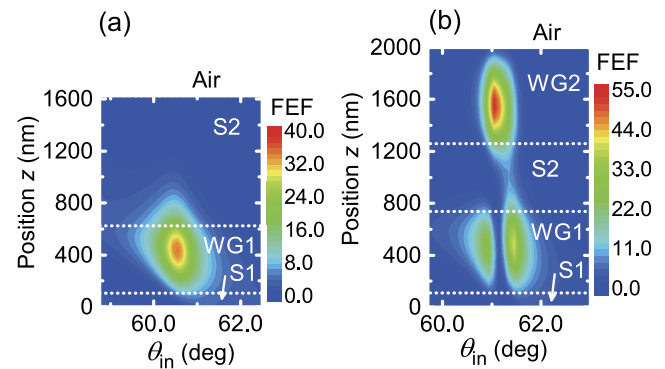
p-pol. emission are essentially the same as those of the *s*-pol. emission shown in Fig. 2(c). As described in detail in the [supplementary material](#), the experimental spectrum can be well fitted by the generalized Fano function proposed by Gallinet and Martin.³¹ Therefore, Fig. 2(c) provides clear experimental evidence of the Fano line shape in the angle-scan fluorescence emission spectrum. The ATR spectrum measured for the same sample with an *s*-pol. probe light is shown in Fig. 2(d). We see a dip accompanied by a shoulder at the large-angle side of the reflectance minimum. Since the ATR measurement was performed under the total reflection condition, the transmittance *T* is zero, and consequently, the absorbance *A* can be obtained by $A = 1 - R$. From a comparison between Figs. 2(c) and 2(d), it is clear that the fluorescence spectrum of the CWG sample exhibits the Fano line shape, while the absorption spectrum is close to a Lorentzian.

We estimated the thicknesses and the refractive indices of the layers by fitting the experimental ATR spectra with theoretical spectra obtained from Fresnel coefficients. As in our previous studies,^{23,26,27,29} we could find sets of parameters that reproduce the experimental spectra quite well. The parameters obtained for the SWG and CWG samples are summarized in Table I. The solid curve in Fig. 2(d) is the EM fit curve obtained from the parameters for the CWG sample; we see that the fit curve reproduces the observed ATR spectrum very well. We could also reproduce well the experimental ATR spectrum of the SWG sample by the parameters listed in Table I. The experimental ATR spectrum is shown in Fig. S2 of the [supplementary material](#) together with a fit curve.

Light emission from emitters placed inside or in the vicinity of photonic structures has been discussed very often based on a classical model of dipole radiation. Within the dipole model, the Lorentz reciprocity theorem is known to provide a simple and powerful tool to analyze the emission properties.^{32–34} The theorem applied to our multilayer structures allows us to state that the *s*-pol. component of power emitted into the prism at an angle θ_{em} by a dipole placed at a position *z* in the WG1 layer, $P_s(\theta_{em}, z)$, is proportional to the square of electric field amplitude $|E_y(z)|^2$ at the same position generated by an *s*-pol. plane wave incident from the prism at an angle $\theta_{in} = \theta_{em}$. Therefore, $P_s(\theta_{em}, z)$ is proportional to the field enhancement factor (FEF) given by $F(z) = |E_y(z)|^2/|E_0|^2$, where E_0 is the amplitude of the incident plane wave. To apply the Lorentz reciprocity to our samples, we calculated $F(z)$ based on a 2×2 transfer matrix method using the parameters listed in Table I. Maps of $F(z)$ obtained for the SWG and CWG samples are shown in Figs. 3(a) and 3(b), respectively. Figure 3(a) clearly demonstrates the

distribution of the enhanced electric field inside the WG1 layer around $\theta_{in} = 60.5^\circ$ with a FEF of ~ 35 . This distribution corresponds to the excitation of the PWG1 mode in the SWG sample. In the CWG sample [Fig. 3(b)], the field distribution inside the WG1 layer is split into two parts separated by a low field enhancement region. In this region, an enhanced field distribution with a maximum FEF of ~ 50 is generated in the WG2 layer.

The map shown in Fig. 3(b) displays clearly the suppression of electric fields in the WG1 layer. This suppression is caused by the coupling of the PWG1 mode with the PWG2 mode. A PWG mode is an EM wave that propagates inside a waveguide (core) layer in an in-plane direction accompanied by evanescent EM fields exponentially decaying away from the core-clad interfaces in out-of-plane directions. In our CWG sample, both the PWG1 and PWG2 modes accompany the evanescent EM fields inside the spacer layer located in between the WG1 and WG2 layers [the S2 layer in Fig. 1(a)]. When the S2 layer is thin enough, the PWG1 and PWG2 modes can interact with each other through their evanescent fields and coupling of the modes takes place. As discussed in depth in our previous paper on the ATR Fano line shapes generated by all-dielectric multilayer structures,²⁷ as a consequence of the mode coupling, EM fields inside the WG1 layer are suppressed at the resonance position of the PWG2 mode, provided that the PWG1 resonance is broad and the PWG2 resonance is sharp, and the coupling is weak enough (thick enough S2 layer). This behavior of the local electric fields inside the WG1

**FIG. 3.** Maps of the calculated FEF for the SWG sample (a) and the CWG sample (b), generated by a plane wave incident on the samples through the prism.

layer is typical in the Fano-resonant multilayer structures and leads to the Fano-resonant optical responses. The map given in Fig. 3(b) demonstrates that the same situation is encountered in the present sample.

Since the DCM molecules are dispersed in the WG1 layer in our samples, to obtain theoretical emission spectra that can be compared with the experimental ones, it is necessary to sum up the power emitted by molecules (radiating dipoles) distributed in a volume excited by the excitation beam. When a uniform distribution of the molecules in the layer is assumed, the power emitted by the ensemble of molecules can be calculated by integrating $P_s(\theta_{em}, z)$ over the volume of the excited spot. Since the fluorescence intensity is detected at a distance far from the excited spot, the variation of θ_{em} depending on the position of the molecules can be neglected. In this case, the integration over the excited volume becomes proportional to the integral of $P_s(\theta_{em}, z)$ with respect to z over the WG1 layer thickness. A justification of this simple treatment is found in the [supplementary material](#). Since $P_s(\theta_{em}, z)$ is proportional to $F(z)$ according to the Lorentz reciprocity, we performed the integration of $F(z)$ over the layer thickness. After integrating $F(z)$ and normalizing to the maximum values, calculated spectra are compared with experimental emission spectra in Figs. 2(b) and 2(c) for the SWG and CWG sample, respectively. These figures demonstrate that the calculated emission spectra agree fairly well with the experimental spectra. These results indicate that the Lorentz reciprocity is an extremely useful tool to predict the emission spectra of emitters embedded in multilayer samples based on simple EM simulations rather than more complicated three-dimensional EM simulations.

The reason why the emission and ATR spectra exhibit different line shapes can be explained as follows. The ATR spectrum is determined by the absorption in the sample. According to the EM theory,³⁵ the absorption at a position z in a layer is proportional to $2n\kappa |E(z)|^2$, where n and κ are the real and imaginary parts of the complex refractive index of the layer and $E(z)$ is the local electric field at z induced by the incident light. We consider the energy flow of light incident on the unit area of the prism-sample interface. To evaluate the energy absorbed in a layer, we take a volume terminated by unit areas on the interfaces at both sides of the layer. The ratio of the energy absorbed in that volume of the layer to the energy of incident light per unit area is given by $C(\cos \theta_{in})^{-1} \int 2n\kappa |E(z, \theta_{in})|^2 / |E_0|^2 dz$, where C is a constant, θ_{in} is the angle of incidence of the ATR probe light (inside the prism), and the integration is taken over the thickness of the layer. The factor $(\cos \theta_{in})^{-1}$ accounts for the variation of the incident energy per unit area. The absorption spectra of respective layers can be calculated using the numerical results of $F(z)$ [Fig. 3(b)] together with the values of n and κ listed in Table I.

In Fig. 4, absorption spectra calculated for respective layers are shown and the total absorption spectrum (summation of all the contributions) is compared with the experimental absorption spectrum obtained from the ATR spectrum [Fig. 2(d)] using $A = 1 - R$. This figure clearly demonstrates that the absorption in the present CWG sample is dominated by that in the SB35-PS (WG2) layer and other contributions are negligibly small. In this figure, the total spectrum appears to be identical to that of the SB35-PS layer and agrees very well with the experimental spectrum. The dominant contribution of the SB35-PS (WG2) layer to the total absorption is due to its value

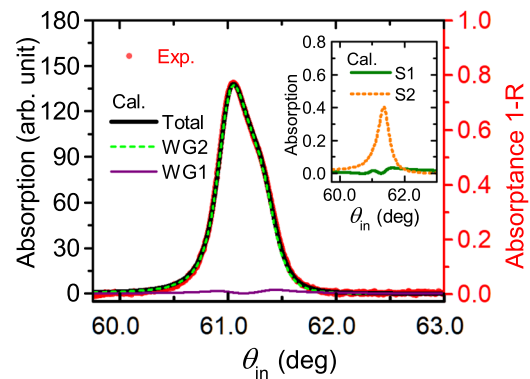


FIG. 4. Calculated absorption spectra of respective layers in the CWG sample for $\lambda = 632.8$ nm (ATR probe light) and total absorption spectrum. The experimental absorption spectrum obtained from the measured ATR spectrum [Fig. 2(d)] using $A = 1 - R$ is also shown.

of $2n\kappa \sim 40$ times larger than that of the WG1 layer and ~ 80 times larger than those of the S1 and S2 layers. Furthermore, the map of $F(z)$ shown in Fig. 3(b) indicates that the local electric fields are the strongest inside the WG2 layer. It is now clear that the line shape in the absorption spectrum (or the ATR spectrum) is determined by the distribution of local electric fields inside the WG2 layer, which is close to the Lorentzian. In contrast, as suggested by the Lorentz reciprocity theorem, the line shape of the fluorescence emission is determined by the electric field distribution inside the WG1 layer. Therefore, the dip seen in the Fano-type fluorescence emission spectrum is due to the suppression of the electric fields in the WG1 layer caused by the coupling of the PWG1 mode with the PWG2 mode, as suggested by the Lorentz reciprocity.

In conclusion, angle-scan fluorescence emission spectra were measured in the reverse ATR geometry for all-dielectric multilayer structures containing a waveguide layer doped with fluorescent dye molecules. The SWG sample containing only one fluorescent waveguide layer showed highly directional emission similar to that observed in surface plasmon-coupled emission, although the sample contained no metallic layer. For the CWG sample in which two PWG modes couple with each other, a Fano line shape was clearly observed. The observed Fano line shape could be very well reproduced by EM calculations based on the Lorentz reciprocity. The Fano-type emission spectrum is a manifestation of the Fano-resonant behavior of local electric fields in the fluorescent waveguide layer resulting from the coupling of the PWG modes. We finally note that similar Fano line shapes can be generated in wavelength-scan fluorescence emission spectra, which are currently under investigation. Together with our recent achievements of light-controllable Fano resonance,^{28,29,36–38} the findings of the present work may pave the way to further develop photofunctional Fano resonances.

See the [supplementary material](#) for the observed p -pol. emission spectrum, the ATR spectrum observed for the SWG sample, and the fitting of experimental angle-scan fluorescence emission spectrum to the generalized Fano function. The justification for a

simplified treatment for integrating the power emitted by an ensemble of dipoles is also given in the [supplementary material](#).

This work was supported by JSPS KAKENHI, Grant Nos. 19K05307 and 16H03828. This work was also partially supported by the Russian Foundation for Basic Research, Grant No. 18-29-20006.

DATA AVAILABILITY

The data that support the findings of this study are available within this article (and its [supplementary material](#)).

REFERENCES

- ¹E. M. Purcell, *Phys. Rev.* **69**, 681 (1946).
- ²R. R. Chance, A. Prock, and R. Silbey, *Advances in Chemical Physics* (John Wiley & Sons Ltd., 2007), pp. 1–65.
- ³W. L. Barnes, *J. Mod. Opt.* **45**, 661 (1998).
- ⁴I. Gryczynski, J. Malicka, Z. Gryczynski, and J. R. Lakowicz, *Anal. Biochem.* **324**, 170 (2004).
- ⁵J. Enderlein and T. Ruckstuhl, *Opt. Express* **13**, 8855 (2005).
- ⁶K. Ray, H. Szmanski, J. Enderlein, and J. R. Lakowicz, *Appl. Phys. Lett.* **90**, 251116 (2007).
- ⁷J. R. Lakowicz, *Plasmonics* **1**, 5 (2006).
- ⁸L. Novotny and N. van Hulst, *Nat. Photonics* **5**, 83 (2011).
- ⁹M. Pelton, *Nat. Photonics* **9**, 427 (2015).
- ¹⁰S. Bidault, M. Mivelle, and N. Bonod, *J. Appl. Phys.* **126**, 094104 (2019).
- ¹¹I. Staude, T. Pertsch, and Y. S. Kivshar, *ACS Photonics* **6**, 802 (2019).
- ¹²T. Baba, H. Makino, T. Mori, T. Hanada, T. Yao, and H.-Y. Lee, *Appl. Phys. Lett.* **87**, 171106 (2005).
- ¹³S. R. K. Rodriguez, S. Murai, M. A. Verschuuren, and J. G. Rivas, *Phys. Rev. Lett.* **109**, 166803 (2012).
- ¹⁴T. Yin, Z. Dong, L. Jiang, L. Zhang, H. Hu, C.-W. Qiu, J. K. W. Yang, and Z. X. Shen, *ACS Photonics* **3**, 979 (2016).
- ¹⁵S. Yuan, X. Qiu, C. Cui, L. Zhu, Y. Wang, Y. Li, J. Song, Q. Huang, and J. Xia, *ACS Nano* **11**, 10704 (2017).
- ¹⁶X. Zhang, S. Choi, D. Wang, C. H. Naylor, A. T. C. Johnson, and E. Cubukcu, *Nano Lett.* **17**, 6715 (2017).
- ¹⁷S. Romano, G. Zito, S. Managò, G. Calafiore, E. Penzo, S. Cabrini, A. C. De Luca, and V. Mocella, *J. Phys. Chem. C* **122**, 19738 (2018).
- ¹⁸S. Liu, A. Vaskin, S. Addamane, B. Leung, M.-C. Tsai, Y. Yang, P. P. Vabishchevich, G. A. Keeler, G. Wang, X. He, Y. Kim, N. F. Hartmann, H. Htoon, S. K. Doorn, M. Zilk, T. Pertsch, G. Balakrishnan, M. B. Sinclair, I. Staude, and I. Brener, *Nano Lett.* **18**, 6906 (2018).
- ¹⁹C. Ayala-Orozco, J. G. Liu, M. W. Knight, Y. Wang, J. K. Day, P. Nordlander, and N. J. Halas, *Nano Lett.* **14**, 2926 (2014).
- ²⁰B. Lee, J. Park, G. H. Han, H.-S. Ee, C. H. Naylor, W. Liu, A. T. C. Johnson, and R. Agarwal, *Nano Lett.* **15**, 3646 (2015).
- ²¹S. Hayashi, D. V. Nesterenko, and Z. Sekkat, *Appl. Phys. Express* **8**, 022201 (2015).
- ²²S. Hayashi, D. V. Nesterenko, and Z. Sekkat, *J. Phys. D: Appl. Phys.* **48**, 325303 (2015).
- ²³S. Hayashi, D. V. Nesterenko, A. Rahmouni, and Z. Sekkat, *Appl. Phys. Lett.* **108**, 051101 (2016).
- ²⁴D. V. Nesterenko, S. Hayashi, and Z. Sekkat, *J. Opt.* **18**, 065004 (2016).
- ²⁵Z. Sekkat, S. Hayashi, D. V. Nesterenko, A. Rahmouni, S. Refki, H. Ishitobi, Y. Inouye, and S. Kawata, *Opt. Express* **24**, 20080 (2016).
- ²⁶S. Hayashi, Y. Fujiwara, B. Kang, M. Fujii, D. V. Nesterenko, and Z. Sekkat, *J. Appl. Phys.* **122**, 163103 (2017).
- ²⁷B. Kang, M. Fujii, D. V. Nesterenko, Z. Sekkat, and S. Hayashi, *J. Opt.* **20**, 125003 (2018).
- ²⁸K. Motokura, B. Kang, M. Fujii, D. V. Nesterenko, Z. Sekkat, and S. Hayashi, *J. Appl. Phys.* **125**, 223101 (2019).
- ²⁹K. Motokura, B. Kang, M. Fujii, D. V. Nesterenko, Z. Sekkat, and S. Hayashi, *J. Appl. Phys.* **127**, 073103 (2020).
- ³⁰B. Kang, K. Motokura, M. Fujii, D. V. Nesterenko, Z. Sekkat, and S. Hayashi, *J. Opt.* **21**, 105006 (2019).
- ³¹B. Gallinet and O. J. F. Martin, *Phys. Rev. B* **83**, 235427 (2011).
- ³²C. E. Reed, J. Giergiel, J. C. Hemminger, and S. Ushioda, *Phys. Rev. B* **36**, 4990 (1987).
- ³³J.-Y. Courtois, J.-M. Courty, and J. C. Mertz, *Phys. Rev. A* **53**, 1862 (1996).
- ³⁴L. Luan, P. R. Sievert, B. Watkins, W. Mu, Z. Hong, and J. B. Ketterson, *Appl. Phys. Lett.* **89**, 031119 (2006).
- ³⁵L. D. Landau and E. M. Lifshitz, *Electrodynamics of Continuous Media*, 1st ed. (Pergamon Press, Oxford, 1960), pp. 253–256.
- ³⁶S. Hayashi, D. V. Nesterenko, A. Rahmouni, H. Ishitobi, Y. Inouye, S. Kawata, and Z. Sekkat, *Sci. Rep.* **6**, 33144 (2016).
- ³⁷S. Hayashi, D. V. Nesterenko, A. Rahmouni, and Z. Sekkat, *Phys. Rev. B* **95**, 165402 (2017).
- ³⁸S. Hayashi, D. V. Nesterenko, and Z. Sekkat, in *Fano Resonances in Optics and Microwaves*, edited by E. Kamenetskii, A. Sadreev, and A. Miroshnichenko (Springer, New York, 2018), pp. 241–260.